

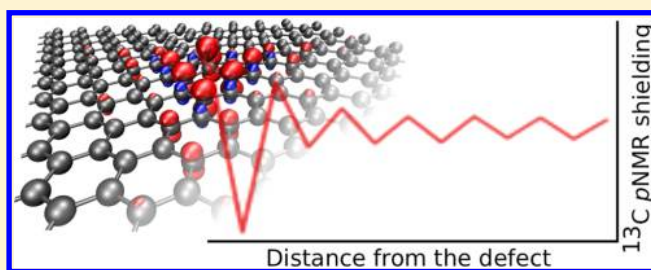
Spin Doublet Point Defects in Graphenes: Predictions for ESR and NMR Spectral Parameters

Jarkko Vähäkangas,* Perttu Lantto, Jiří Mareš, and Juha Vaara*

NMR Research Group, University of Oulu, P. O. Box 3000, FIN-90014 Oulu, Finland

S Supporting Information

ABSTRACT: An adatom on a graphene surface may carry a magnetic moment causing spin-half paramagnetism. This theoretically predicted phenomenon has recently also been experimentally verified. The measurements of defect-induced magnetism are mainly based on magnetometric techniques where artifacts such as environmental magnetic impurities are hard to rule out. Spectroscopic methods such as electron spin resonance (ESR) and paramagnetic nuclear magnetic resonance (pNMR) are conventionally used in the development of magnetic materials, *e.g.*, to study paramagnetic centers. The present density functional theory study demonstrates with calculations of the ESR *g*-tensor and the hyperfine coupling tensors, as well as the pNMR shielding tensor, that these spectroscopies can be used to identify the paramagnetic centers in graphenes. The studied defects are hydrogen and fluorine adatoms on sp^2 -hybridized graphene, as well as hydrogen and fluorine vacancies in the sp^3 -hybridized graphane and fluorographane, respectively. The directly measurable ESR and pNMR parameters give insight into the electronic and atomic structures of these defects and may contribute to understanding carbon-based magnetism via the characterization of the defect centers. We show that missing hydrogen and fluorine atoms in the functionalized graphane and fluorographane, respectively, constitute sp^2 -defect centers, in which the magnetic resonance parameters are greatly enhanced. Slowly decaying adatom-induced magnetic resonance parameters with the distance from the sp^3 -defect, are found in pure graphene.



1. INTRODUCTION

Chemical modifications by adatoms and other kinds of point defects in graphene alter the electronic band structure by creating local magnetic moments into the nonmagnetic, pristine graphene. For example, adatom-induced magnetism of graphene is known and intensively studied both theoretically^{1–8} and experimentally.^{9–15} The ambition in these studies is to create technologically important, nonmetallic magnets and at the same time to understand the origin of magnetism in such carbon-based systems, which can *a priori* be considered to feature only diamagnetic behavior. Magnetism in graphene can arise, besides from individual adatoms, from other lattice imperfections such as vacancies or moieties of adsorbed atoms.¹⁶ All such defects have local magnetic moments which can give rise to magnetic ordering. Recently it was experimentally observed that fluorine adatoms on graphene carry magnetic moments corresponding to spin 1/2.¹¹ While the spin-half paramagnetism is convincingly demonstrated in magnetization measurements, the subject of ferromagnetism due to the magnetic moments in graphene is still controversial. Not only the possibility of ferromagnetic order but also questions remain, such as, how far in the two-dimensional graphene lattice is the influence of the defect mediated?¹⁶ To understand the scenario of the magnetism of graphene, precise identification and characterization of the induced point defects play an essential role.

Experimental evidence of the defect-induced magnetism of graphene is hitherto mainly based on magnetometry measurements by superconducting quantum interference devices.^{9–11,14} Such measurements can only give information on the total magnetic moment, whereas artifacts from unwanted contamination such as environmental magnetic impurities are hard to rule out.^{12,17} In order to probe the magnetic moments on a graphene sheet locally, charge-based transport¹⁷ and scanning tunneling microscopy¹⁸ (STM) measurements have been applied. A spin transport technique that directly probes the intrinsic spin contribution to the magnetic moment has also been used recently.¹² One of the most powerful spectroscopy techniques for obtaining such local information on paramagnetic defects in solids is electron spin resonance (ESR),^{19,20} which has not been yet fully exploited in graphene research.²¹ The characterization capability of the method has been shown, *e.g.*, in ref 22, where low-temperature superparamagnetic-like states were observed via ESR measurements of graphene flakes containing extended defect structures, originating from heavily sonicated nanographite samples. In ref 22, density functional theory (DFT) modeling of the defects was also carried out, with the finding that hydrogen adatoms on graphene are associated with a significant magnetic moment. Similar findings

Received: April 30, 2015

Published: July 7, 2015

were made already in the 2007 DFT study by Yazyev and Helm on the same defect system, as well as paramagnetic single carbon vacancy in graphene.¹ More recently in ref 21, a combined study by ESR and STM, such vacancies were observed in graphene samples which were bombarded by low-energy Ar⁺ ions. Spin dynamical and relaxation processes of spin states of graphene nanoribbons were investigated by means of ESR in ref 23.

ESR is an analytical spectroscopic technique for systems with unpaired electrons, which gives insight into the atomic and electronic structure of material defects. Another spectroscopic technique that nowadays plays a central role in the development of new magnetic materials is paramagnetic nuclear magnetic resonance (pNMR).²⁴ Whereas conventional NMR deals with electronically closed-shell systems, pNMR is used for molecules and materials with unpaired electrons. Traditionally, pNMR is used when the information obtained by ESR is scarce, e.g., in molecules with integer electron spin quantum number *S* or small electron spin densities and, therefore, small hyperfine coupling constants (HFCs).²⁵ Besides these two methods, the so-called muon spin resonance (muSR) technique has also been used for probing magnetism in chemically derived graphene samples.²⁶

The purpose of the present study is to demonstrate that the spectroscopic parameters of ESR (*g*-tensor and HFCs) and pNMR (the shielding tensor), based on as accurate as currently possible periodic first-principles calculations, open the door for an unambiguous identification of defect structures and provide an alternative characterization route to aid in tailoring the magnetic properties of these carbon-based materials. These directly experimentally measurable parameters provide answers to issues such as the range of the influence of the defect into its neighborhood and which atoms are involved with the defect.

In this study, two different kinds of point defects are considered. First, we study vacancies in sp³-hybridized graphenes that have been functionalized with hydrogen (graphane) and fluorine (fluorographene), respectively. We use here the acronyms V_H@HG and V_F@FG for these systems. The second type of defect considered is constituted by hydrogen and fluorine adatoms on a pure, sp²-hybridized graphene sheet, with acronyms H@G and F@G, respectively. Both kinds of defects carry a magnetic moment corresponding to spin-1/2, and constitute paramagnetic centers in the corresponding graphenic materials. Our calculations are based on DFT and periodic boundary conditions, where the defect concentration can be practically controlled with the size of the supercell containing one defect. By these calculations we are able to monitor the efficiency by which the unpaired spin density is conveyed to the material from the defect, as revealed by the ESR and pNMR parameters.

2. THEORY

2.1. ESR Parameters. The most important ESR spectral parameter is the *g*-tensor, which corresponds to the Zeeman interaction of the magnetic moments of the paramagnetic defects with the externally applied magnetic field in the ESR experiment. Such interactions are sensitive to the local geometric and electronic structure. The *g*-shift tensor is defined as the difference $\Delta\mathbf{g} = \mathbf{g} - g_e\mathbf{1}$ from the isotropic free-electron *g*-factor, $g_e = 2.002319304$. The HFC tensor, **A**, contains the contact and dipolar coupling between the electronic and nuclear spins and contributes to the fine structure of the ESR

spectrum. The experimental spectrum of the present spin-1/2 defect centers can be interpreted in terms of the Hamiltonian

$$H_{\text{eff}} = \mu_B \mathbf{B} \cdot \mathbf{g} \cdot \mathbf{S} + \sum_K \mathbf{S} \cdot \mathbf{A}_K \cdot \mathbf{I}_K \quad (1)$$

where the Zeeman interaction term is bilinear in the effective electron spin **S** and the applied uniform magnetic field **B**, and the HFC term with **S** and the nuclear spins **I_K**. Here, μ_B is the Bohr magneton and the sum runs over the magnetic nuclei *K*.

A method for calculating the *g*-tensor in extended systems using periodic boundary conditions and the pseudopotential formalism has been developed by Pickard and Mauri.²⁷ It is based on the gauge-including projector augmented wave (GIPAW)²⁸ ansatz that can be regarded as an extension of Blöchl's PAW method.²⁹ To evaluate the *g*-shift tensor, which has its physical origin in the spin-orbit interaction, magnetic response currents are needed.²⁷

In contrast to the *g*-tensor, which is a second-order response property, HFC is a ground-state property. In the PAW-based method by Van de Walle and Blöchl,^{30,31} HFC can be calculated from the density difference of the spin-up and spin-down electrons, n_\uparrow and n_\downarrow . At the nonrelativistic (NR) limit, the **A**-tensor consists of a sum of two physically different terms. The isotropic component arises from the Fermi contact (FC) interaction¹⁹ that is only sensitive to the *s*-electron density located at the nucleus. The other, spin-dipole (SD) term, has an anisotropic character and is sensitive particularly to the *p*-electron contribution to the density near the nucleus. These hyperfine interactions were studied by hybrid DFT computations in small, ionic graphene *S* = 1/2 radicals in ref 32. The local nature of hyperfine interactions was pointed out in ref 32 as a basis for extrapolating the results obtained for small graphenic models to more extended structures.

2.2. pNMR Shielding. As compared to the standard NMR of closed-shell substances, in pNMR the chemical shifts are greatly enhanced, thus providing a kind of “magnifying glass” for paramagnetic systems. This enhancement arises from the interaction of the nuclear spins with the large magnetic moment of the unpaired electron(s).²⁵ In pNMR, an ensemble of $2S + 1$ thermally populated states needs to be considered. Besides the orbital contributions to the shielding tensor of nucleus *K*, σ_K^{orb} , which is analogous to the shielding tensor of diamagnetic systems, one has to consider the temperature-dependent hyperfine shielding, which arises from the spin-dependent FC and SD hyperfine interactions.¹⁹ The total shielding tensor in the case of a spin-half paramagnetic system can be written as³³

$$\sigma_K = \sigma_K^{\text{orb}} - \frac{1}{\gamma_K \hbar} \frac{\mu_B}{kT} \frac{S(S+1)}{3} \mathbf{g} \cdot \mathbf{A}_K \quad (2)$$

where the ESR parameters **g** and **A_K** may be analyzed in terms of relativistic corrections arising, for the present light-atom systems, primarily from the spin-orbit (SO) interaction. The corrections can be classified according to their order in the fine structure constant α , with terms up to the fourth order, $O(\alpha^4)$, typically retained.^{33,34} The expansions of **g** and **A** and the resulting shielding terms in eq 2 are detailed in the Supporting Information (SI). Table 1 lists the presently considered hyperfine shielding terms for the *S* = 1/2 defect systems.

Table 1. Hyperfine Shielding Terms Resulting from the Product $g \cdot A_K$ in Equation 2 with the Order of the Fine Structure Constant α and the Tensorial Rank, to Which the Term Contributes, in a Spin-Half Paramagnetic System

$g \cdot A_K^a$	nature of the term	order in α	tensorial rank ^b
$g_e A_{\text{con}}$	nonrelativistic contact	α^2	0
$g_e A_{\text{dip}}$	nonrelativistic dipolar	α^2	2
$\Delta g_{\text{iso}} A_{\text{con}}$	contact term from SO contribution to g	α^4	0
$\Delta g_{\text{iso}} A_{\text{dip}}$	dipolar term from SO contribution to A	α^4	2
$\Delta \tilde{g} A_{\text{con}}$	anisotropic contact	α^4	2
$\Delta \tilde{g} A_{\text{dip}}$	pseudocontact	α^4	0, 2

^a g_e is the free-electron g -factor, A_{con} and A_{dip} are the isotropic and dipolar hyperfine couplings, and Δg_{iso} and $\Delta \tilde{g}$ are the isotropic and anisotropic parts of the g -shift tensor. It should be noted that, of the terms listed for the $S = 1/2$ case in ref 34, we have presently omitted those arising from the SO corrections to A_K , which are very small for light-atom systems of the present kind. ^bThe rank-0 contribution corresponds to the isotropic shielding constant (chemical shift) and the rank-2 contribution to the anisotropic but symmetric part of shielding.

3. COMPUTATIONAL DETAILS

The considered defect models were treated using periodically repeated hexagonal graphene supercells. An 18 Å thick vacuum layer in the z -direction perpendicular to the material layer was used to minimize interlayer interactions. In the xy -plane containing the material layer, supercell sizes $n \times n$ were considered, where $n = 3, 6, 9, 12$ depict the numbers of the complete hexagons of the two-dimensional hexagonal lattice.

The different supercells made it possible to consider the convergence of the ESR and pNMR parameters with the system size. In terms of concentration, the vacancy concentration varied from 5.6% to 0.6% and the adatom concentration from 5.6% to 0.3%. These choices of supercell parameters were based on our previous work,³⁵ where the NMR parameters were predicted for defect-free, diamagnetic G, HG, and FG materials. The optimized lattice constant values of these systems are 2.466, 2.535, and 2.603 Å, respectively, as obtained in periodic DFT calculation³⁵ with the generalized gradient approximation functional, PBE.³⁶ These lattice constants were used to build supercells containing either one missing atom in the $V_{\text{H}}@HG$ and $V_{\text{F}}@FG$ models, or one adatom in the $\text{H}@G$ and $\text{F}@G$ models. The defect models were structurally optimized with the lattice constants kept fixed and only letting the atomic positions relax. The optimizations as well as the calculations of the ESR parameters were performed on the Quantum Espresso package³⁷ using DFT with spin-polarized PBE. In the geometry optimization, ultrasoft pseudopotentials³⁸ were used and the Kohn–Sham orbitals were expanded on a plane-wave basis set limited by a kinetic energy cutoff of 50 Ry. In contrast, in the ESR calculations the so-called norm-conserving pseudopotentials³⁹ were used with a 90 Ry cutoff. Monkhorst–Pack-type⁴⁰ of Γ -point-centered k -point meshes were used in both types of calculations for Brillouin zone integration. The required spacing between the grid points in the reciprocal space in the x and y directions was 0.03902 \AA^{-1} both in the geometry optimization and ESR calculations for the $V_{\text{H}}@HG$ and $V_{\text{F}}@FG$ vacancy defect cases, whereas the remarkably tight 0.00650 \AA^{-1} spacing

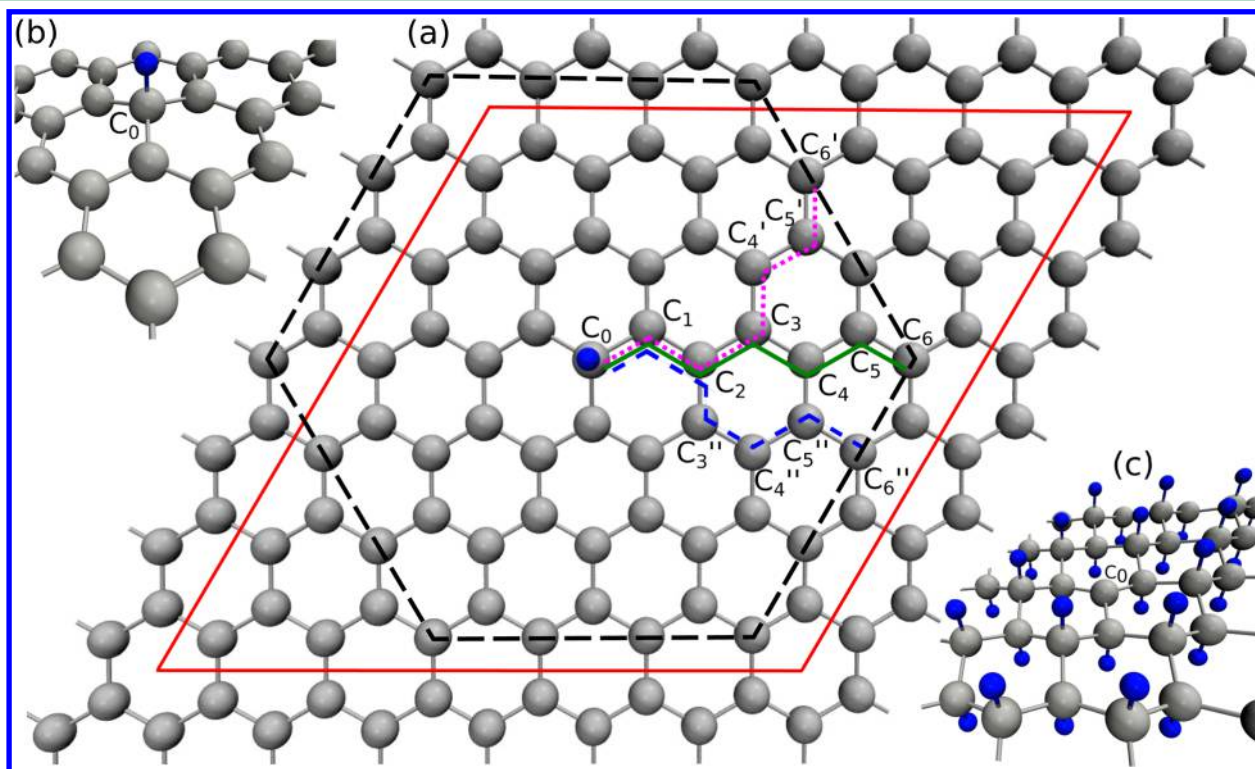


Figure 1. (a) Optimized structure of an H adatom-induced defect in a 6×6 unit cell of graphene. The unit cell is shown with full lines and the corresponding Voronoi cell by the dashed lines. Symmetry-independent ^{13}C sites are labeled with numbers increasing from the carbon site with the adatom (C_0). This work reports ESR hyperfine couplings and pNMR shieldings for the nuclei C_i along the solid green and the two dashed (blue and pink) lines. Inset b highlights the region with H or F adatom in the sp^2 -hybridized graphene sheet ($\text{H}@G$ and $\text{F}@G$), whereas in inset c the vacancy-type defect in hydrogenated/fluorinated sp^3 -hybridized graphene ($V_{\text{H}}@HG$ and $V_{\text{F}}@FG$) is illustrated.

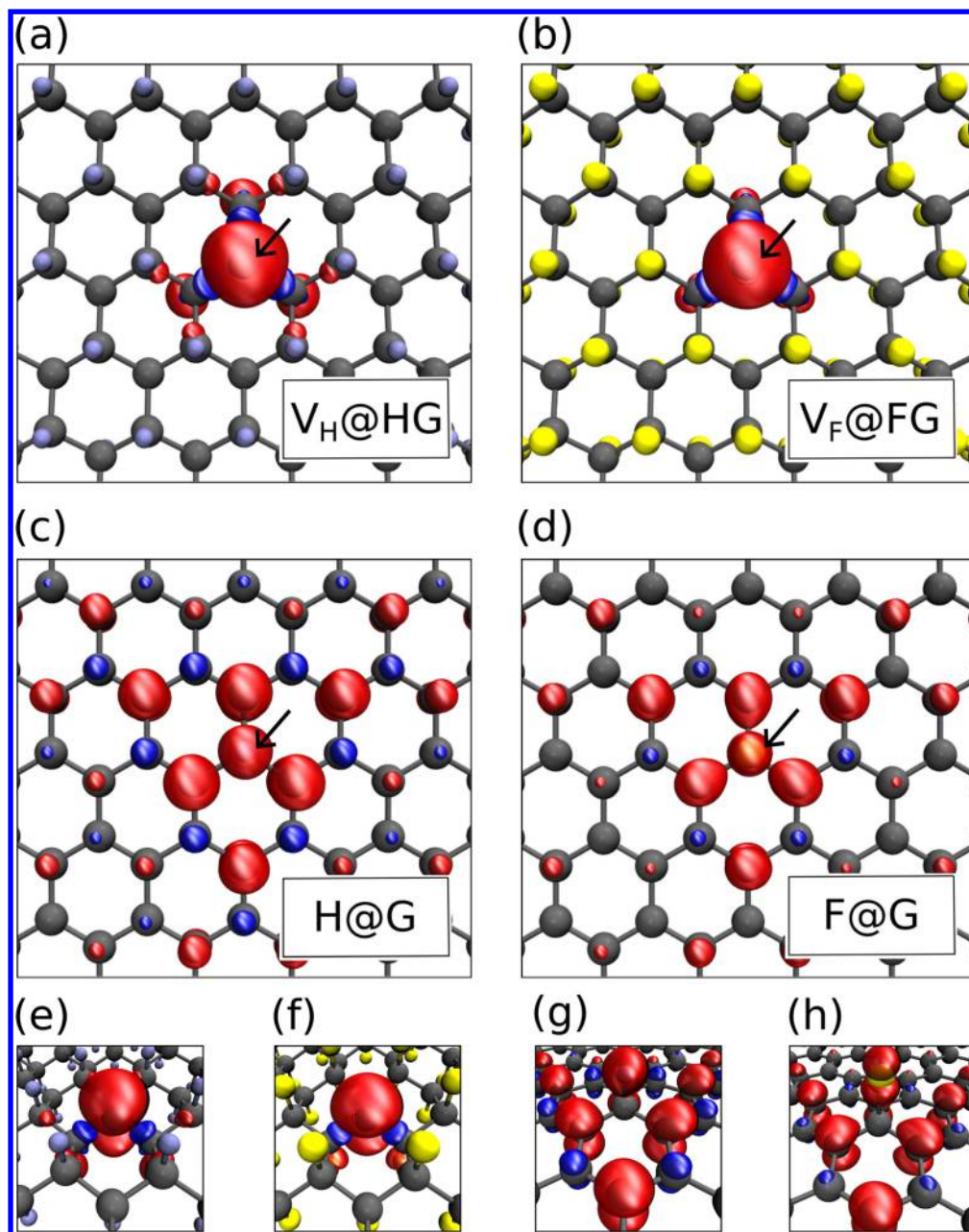


Figure 2. Spin densities of models for (a) hydrogen vacancy in graphane ($V_H@HG$), (b) fluorine vacancy in fluorographane ($V_F@FG$), (c) hydrogen adatom on graphene ($H@G$), and (d) fluorine adatom on graphene ($F@G$) systems with supercell size of 6×6 . The arrows indicate the location of the defect. The same quantities are shown in e–h from the side perspective, in the corresponding order. The majority (minority) spin density component is shown in red (blue) with the isosurface value of 0.02 (-0.02) $e/\text{\AA}^3$.

was needed in the cases of $H@G$ and $F@G$, the adatom-defected graphene supercells, due to the sp^2 hybridization. These k -point grids, together with the 5×10^{-3} eV/ \AA convergence threshold on the residual forces in the optimized structure, led to less than 1×10^{-4} \AA numerical displacement error in the atomic positions and less than 1% numerical error in the ESR parameters.

4. RESULTS AND DISCUSSION

4.1. Defects and Their Spin Density Distributions.

Figure 1a depicts the relaxed structure of the adatom-induced defect in the size 6×6 unit cell, as well as the corresponding Voronoi cell that indicates the carbon atoms that are equidistant from the defects that are located at the centers of

the adjacent supercells. Additionally, ^{13}C centers within the Voronoi cell are labeled with the number of CC-bonds as counted from the carbon atom C_0 , at which the defect is located. Centers along three different bonding pathways (colored in the figure) are followed in the present inspection of the site-specific parameters, the ESR A-tensor and the pNMR shielding tensor. Figure 1b shows a three-dimensional view of the structure around a hydrogen adatom and the directly bonded sp^3 -hybridized carbon atom, C_0 . The displacements of the neighboring C_1 atoms are very small. Similar finding holds also in the F-chemisorbed case. The corresponding view of the $V_H@HG$ system containing C_0 , which hosts the hydrogen vacancy, is shown in Figure 1c, where the zigzag layer

is locally rendered almost planar at the location of the sp^2 -hybridized C_0 atom.

Both types of point-defected systems discussed here give rise to quasi-localized states in the vicinity of the Fermi level. This is illustrated in Figure S1 in the SI, where the densities of states (DOS) for all of the systems are plotted. In the two predominantly sp^3 -hybridized vacancy defect cases (SI Figure S1a,b) there is a clear energy gap with well-separated spin-up and -down impurity states either both in the band gap ($V_H@HG$) or in $V_F@FG$, with the occupied spin-up state in the valence band and the unoccupied spin-down state in the gap. Also in both chemisorbed cases, $H@G$ and $F@G$, distinct spin-polarized defect states exist in the immediate vicinity of the Fermi level (SI Figure S1c,d). In these primarily sp^2 -hybridized systems, the energy gap is small. With supercells of increasing size and, therefore, larger spatial separation of the defects, the DOS of the defected model approaches that of pristine, zero-gap graphene. This development is shown in Figure S2 of the SI. A common feature that all of the present systems share is the bipartite lattice, which can be regarded as consisting of two interpenetrating hexagonal carbon sublattices, α and β . The bipartite character leads to a situation where a defect created, e.g., in the α -lattice, brings about a quasi-localized state formed only from the p_z -orbitals of the β -carbon atoms, and *vice versa*.¹ The so-called $(\sqrt{3} \times \sqrt{3})R30^\circ$ superstructure can be recognized in scanning tunneling microscopy images up to distances of several nanometers around the defects.^{1,41–43}

Figure 2 demonstrates that the studied defected graphenes possess the known 3-fold symmetry of the spin density of the $\sqrt{3}$ -structure systems.^{1,41–43} The sp^3 -hybridized vacancy systems feature a clearly localized character of the spin distribution, consistent with a large band gap, as illustrated by Figure 2a,b. The locally sp^2 -hybridized defect centers have a large majority spin density contribution whereas the C_1 atoms in the adjacent (β) sublattice carry a small minority spin density. On the other hand, in the adatom cases the defect generates a long-range spin polarization in both the $H@G$ and $F@G$ systems, Figure 2c,d. This arises not only due to the sp^2 -hybridized bipartite structure but more importantly from the exchange splitting of the defect states (in the so-called exchange-polarization effect^{1,32}), which can be regarded as the response of the fully populated valence bands to the magnetization of the defect states. There is a slowly decaying majority spin density at the odd-nearest-neighbor sites ($C_{1,3,5,\dots}$), referring to the numbering in Figure 1a, and a similarly decaying minority spin density occupying the even-indexed-neighbor sites ($C_{2,4,6,\dots}$). Another difference between the sp^2 -defect (vacancy in substituted sp^3 -graphenes) and sp^3 -defect centers (adatoms in sp^2 -graphene) is that the C_0 atom possesses a huge majority of the spin density in the vacancy systems whereas no such dramatic maximum of the spin density can be found on the C_0 of the adatom systems.

4.2. ESR Parameters. Figure 3 depicts the isotropic g -value as a function of the size $n \times n$ of the supercell (the numerical values of these as well as the data of other figures are tabulated in the SI). The vacancy-defected, sp^3 -hybridized systems possess completely converged values. For the $V_H@HG$ system, the result of 2.00262 is obtained already with the smallest (3×3) supercell size, whereas, for $V_F@FG$, the value of 2.00253 is reached with the 6×6 supercell. These values originate from the very localized spin densities (*vide supra*) in these systems that feature a well-defined band gap. A large drop of the g -value in $V_F@FG$ from the 3×3 model to the converged value in the

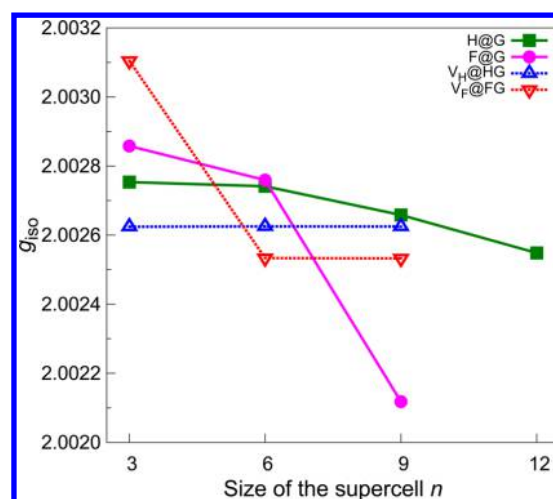


Figure 3. Isotropic g -value as a function of the size of the supercell, where the x -axis indicates n in the $n \times n$ supercell. The chemisorbed defect systems $H@G$ and $F@G$ are shown as solid lines, and the vacancy systems $V_H@HG$ and $V_F@FG$ as dashed lines. Corresponding anisotropic ($g_{\perp} - g_{\parallel}$) values are shown in Figure S3 in the SI.

bigger system sizes can be attributed to the couplings between the periodic images of the defect in the 3×3 model. In complete contrast, the systems with adatom defects feature no similar type of convergence with the model size. These systems, $H@G$ and $F@G$, have a delocalized spin density, and their band gaps decrease with the model size, hindering the stable calculation of this second-order material property. The latter point is illustrated for $H@G$ in Figure S2 of the SI. As illustrated in Figure S3, also in the SI, converged tensor components are obtained for the g -tensor for $H@G$ with the 3×3 system size, but only using the extremely dense $24 \times 24 \times 1$ k -point sampling. Due to the excessive computational cost, a similar convergence study was not pursued for $F@G$. The demand for dense k -sampling arises from the previously mentioned defect states close to the Fermi energy. Their separation decreases together with the bandgap when the distance between the defects increases (*vide supra*). This means that it is only possible to obtain sufficient k -sampling for a given, small supercell size and, hence, defect concentration, as tested with the 3×3 supercell (SI Figure S4). This becomes ultimately unfeasible for well-separated defects, where the situation resembles more and more that in the zero bandgap, pristine graphene. As noted earlier, the second-order nature of this property requires an energy gap in calculations of the present kind. Without such a feature, second-order properties fail to converge as functions of k -sampling, as has been demonstrated for the NMR shielding constant of graphene.³⁵ The presently reported values with the 3×3 supercell size for the g -tensor in $H@G$ and $F@G$ have, consequently, relevance only for the very high defect concentration represented by this system size.

The results (Figure 3) for the isotropic g -factor of the $H@G$ and $F@G$ systems, albeit not entirely converged due to the preceding reasons, are in good agreement with the experimental magnitude in the range $g = 2.001 - 2.003$ obtained for carbon vacancy,²¹ another type of point defect in graphene. In the present study, relative anisotropies of the g -tensor of around 0.05% (SI Figure S3) are obtained for the adatom defects, to be compared with 0.02% for the carbon vacancies reported in ref 21. An additional difference prevails in the sign of the

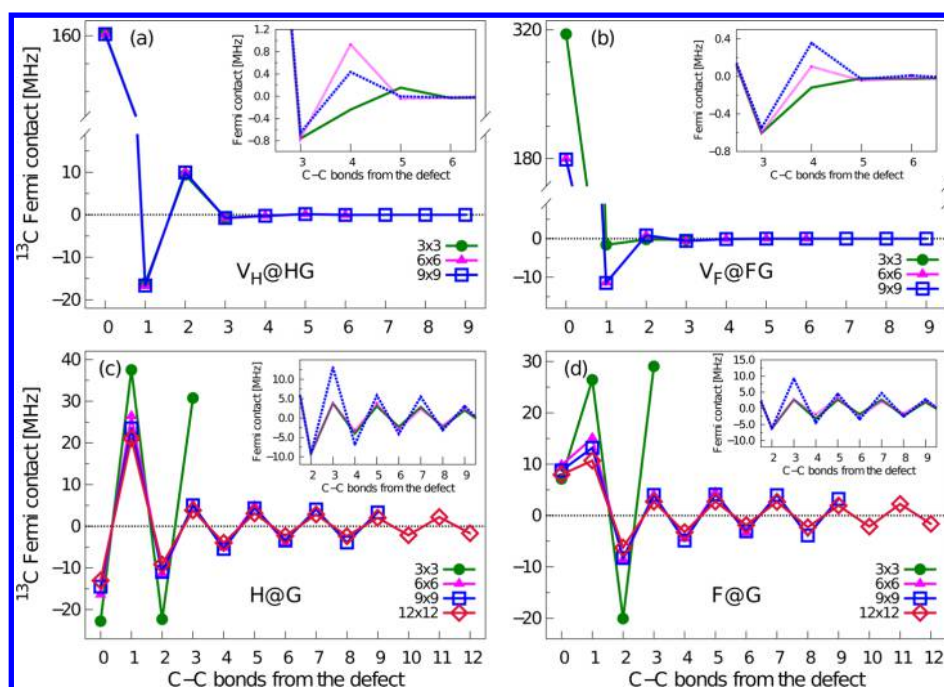


Figure 4. Isotropic hyperfine coupling constant (MHz), *i.e.*, the Fermi contact contribution to the A-tensor, for carbon-13 nuclei as a function of the distance from the defect site for graphene models hosting a single point defect: (a) $V_H@HG$, (b) $V_F@FG$, (c) $H@G$, and (d) $F@G$. In the main plots, the bonding pathway colored with green in Figure 1 is plotted, and the insets highlight symmetry-independent atomic sites along different bonding paths. The numbering of CC-bonds and color encoding in the insets match those in Figure 1. The $n \times n$ configuration for the main panels refers to the different supercell sizes used.

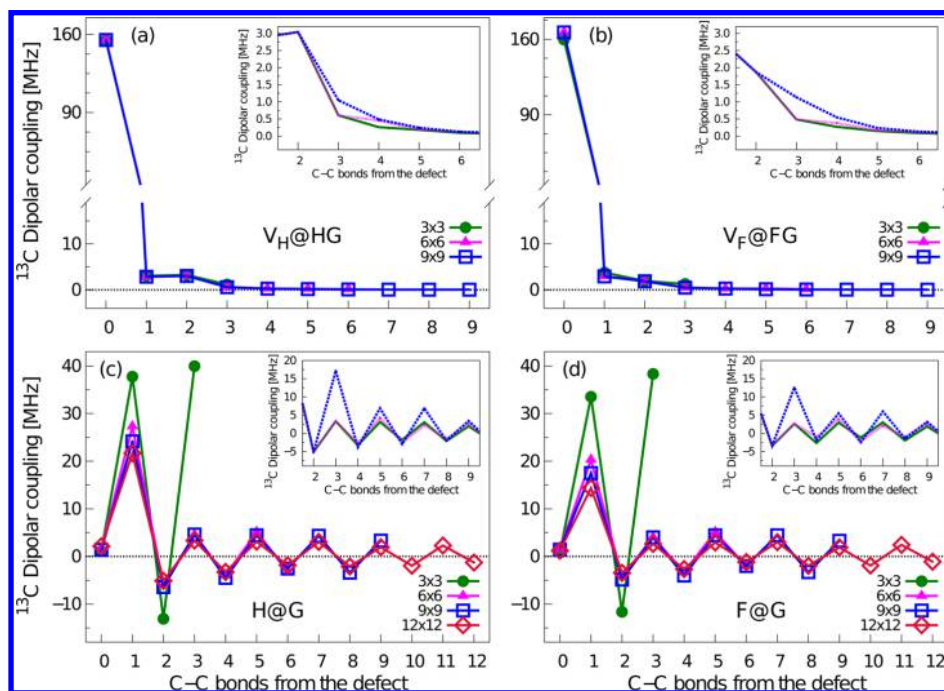


Figure 5. Same as Figure 4 but for the anisotropic part, dipolar hyperfine coupling. The unique principal value ($A_{33}^{SD} = A_{\perp}^{SD}$), of the dipolar hyperfine tensor, is illustrated.

anisotropy: For the adatom-defected graphenes the in-plane g-tensor component is larger than the perpendicular component, a situation opposite to that prevailing for carbon vacancies according to ref 21.

The isotropic HFCs of the carbon nuclei of the four presently considered defect systems as functions of the number of bonds from the defect site are shown in Figure 4. The plots

of sp^3 -hybridized vacancy systems in Figure 4a,b highlight the localized nature of the paramagnetic center in these cases. The $V_H@HG$ system shows similar results for all of the supercell sizes, as in the case of g-tensor, suggesting that the vacancy defects are noninteracting already at the separation of 7.6 Å corresponding to the smallest, 3×3 supercell. The single sp^2 -hybridized carbon atom right at the defect site possesses a very

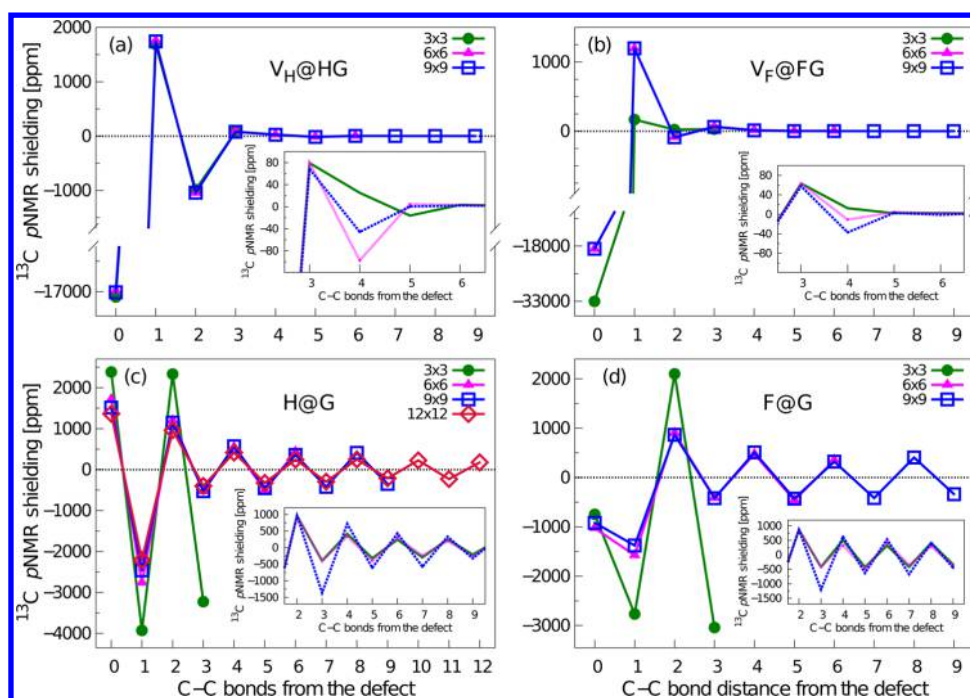


Figure 6. Isotropic part of the paramagnetic ^{13}C shielding (ppm) as a function of the distance (number of CC-bonds) from the defect in the following models: (a) $\text{V}_\text{H}@\text{HG}$, (b) $\text{V}_\text{F}@\text{FG}$, (c) $\text{H}@\text{G}$, and (d) $\text{F}@\text{G}$, respectively. Labels and insets are the same as those in Figures 4 and 5.

large HFC of 160 MHz. The HFC values of the other carbons decrease rapidly with the number of CC-bonds from the defect: For C_1 , the HFC has decayed to the negative value of -18 MHz, and for C_2 , HFC is the positive 10 MHz. Carbon centers further away from the defect site have negligible HFC in $\text{V}_\text{H}@\text{HG}$. A glance into the insets for the $\text{V}_\text{H}@\text{HG}$ as well as $\text{V}_\text{F}@\text{FG}$ systems reveals the fact that the HFC values along different bonding pathways differ relatively little from each other; only at the atomic sites C_4 are slightly differing values obtained. Similarly to what was observed for the convergence of the g -values in $\text{V}_\text{F}@\text{FG}$, the HFC results obtained with the 3×3 supercell deviate strongly from those of the two larger system sizes that, in turn, have similar converged values for the sp^2 -hybridized nucleus at the defect center, C_0 . This indicates that, in contrast to $\text{V}_\text{H}@\text{HG}$, the fluorine vacancies in $\text{V}_\text{F}@\text{FG}$ are still interacting at the 3×3 supercell size. Almost a 2-fold value is obtained at C_0 at the 3×3 system size as compared to the bigger models, which can be understood to result from the defect centers being connected via the bonding network with their periodic replicas. Similarly to $\text{V}_\text{H}@\text{HG}$, almost zero HFCs are obtained for the atomic sites further away, reflecting the tight localization of the spin density around the C_0 and C_1 sites.

The delocalized spin density of the sp^2 -hybridized adatom-defect systems is reflected in the strong, very slowly decaying oscillation of the HFC, with the sign alternating as a function of the number of CC-bonds from the defect. The $\text{H}@\text{G}$ (Figure 4c) and $\text{F}@\text{G}$ (Figure 4d) systems feature similar characteristics in the distance behavior of the ^{13}C HFC. The only remarkable difference between these two systems is the value of HFC at the sp^3 -hybridized C_0 center, circa -15 MHz in $\text{H}@\text{G}$ and 8 MHz in $\text{F}@\text{G}$. The values at the C_1 site in the bigger systems are also almost twice as large in $\text{H}@\text{G}$ as in $\text{F}@\text{G}$. This relates trivially to the spin density shown in Figure 2, where the C_1 center possesses a higher majority spin density in the $\text{H}@\text{G}$ system.

Figure 5 depicts the dipolar HFC coupling in the four defect systems. The plots are, on the one hand, qualitatively similar for the two vacancy systems and, on the other hand, for the two adatom systems. $\text{V}_\text{H}@\text{HG}$ and $\text{V}_\text{F}@\text{FG}$ behave similarly, featuring an equally fast but this time a monotonically decaying dipolar contribution, unlike in the case of the isotropic HFC. Only right at the sp^2 -hybridized defect center (the C_0 site), the HFC possesses a remarkably large value, 150 MHz. This illustrates that almost all of the p -character of the spin density, essential for dipolar HFC, is localized there. In the adatom systems, the dipolar HFC has the same weakly damped character that was seen for the isotropic HFC. The $\text{H}@\text{G}$ and $\text{F}@\text{G}$ systems differ only for the C_1 nuclei, where $\text{H}@\text{G}$ has a slightly bigger dipolar HFC. At the C_0 site, the same small value is obtained in both $\text{H}@\text{G}$ and $\text{F}@\text{G}$, due to the practically vanishing spin density. The insets reveal the fact that the only remarkable difference in the dipolar HFCs between the different symmetry-independent bonding pathways occurs at the C_3 atomic site.

In general, this inspection demonstrates that not only the isotropic contribution but also the anisotropy of HFC is extremely delocalized at the sp^3 -defects of otherwise sp^2 -hybridized parent systems. The different sublattices have anisotropic HFCs values of opposite signs. The alternating signs as well as magnitudes agree qualitatively with the study of HFCs in small graphenic ion radicals,³² as well as the calculated spin densities for the $\text{H}@\text{G}$ defect in ref 1. The alternation between the different sublattices (even- and odd-numbered nearest-neighbor indices) is attributed to the exchange-polarization effect, as discussed in ref 1. The strong coupling between defects due to the delocalized electron densities in $\text{H}@\text{G}$ and $\text{F}@\text{G}$ systems is clearly revealed in both the isotropic and anisotropic ^{13}C HFC values of the smallest 3×3 unit cell. In addition to this, the same parameters for the closest nuclei to the defect, C_1 and to some extent also C_2 , show a

dependence on the unit cell size, *i.e.*, the separation of the defects.

4.3. pNMR Shielding. A glance at Figure 6, which presents the isotropic pNMR shielding constants, reveals the previously mentioned magnifying-glass character of the unpaired electron spin in pNMR experiments. All of the presently considered systems possess huge shielding constant values in the vicinity of the defect center. In $V_H@HG$ and $V_F@FG$ systems, the C_0 nucleus is highly deshielded, as shown in Figure 6a,b. Instead, in the adatom system $H@G$, the C_0 nucleus is shielded but the corresponding nucleus in $F@G$ is deshielded. These findings and the overall behavior of the shielding constants are in a striking accordance with the corresponding isotropic HFC values, shown in Figure 4. The fact that these quantities feature similar trends arises ultimately from the spin density distribution. It should be noted that the NMR signal of nuclei close to the defect site is not likely to be observable in practice, due to the rapid relaxation rate and, hence, extreme line broadening at these sites.²⁴ In contrast, nuclei further away from the defect may give sharp lines. Furthermore, the only significant contribution to the hyperfine shielding arises from the term 1 in Table 1, *i.e.*, the product of the free-electron g_e -factor and the isotropic Fermi contact HFC, other terms contributing less than 1 ppm. This gives us at least a partial justification for dropping off the $O(\alpha^4)$ terms in the cases of the adatom systems, $H@G$ and $F@G$, for which it is exceedingly difficult to obtain converged g -tensors. For the $V_H@HG$ and $V_F@FG$ systems that have a finite band gap even at the limit of infinitely separated defects, also those terms converge to definite values. However, the contribution of the terms involving $\Delta\tilde{g}$ is negligible to shielding in these systems. The shielding anisotropy is illustrated in Figure S5 in the SI. The only significant contribution to $\Delta\sigma$ comes from the term 2, the leading $O(\alpha^2)$ order term determined by the dipolar coupling tensor, A_{dip} .

Generally, it is demonstrated that the pNMR shielding (and, therefore, the chemical shift) is tremendously enhanced for the carbon nuclei in the vicinity of the defect centers, reflecting their paramagnetic nature. In chemisorbed graphenes, Figure 6c,d, the bipartite lattice and the delocalized spin density distribution cause enhanced, long-ranged shielding values alternating in sign for carbon nuclei around the sp^3 -defect center. This provides characteristic spectral features that identify different adatom defects and also information about the defect density. The fact that the main contributions to paramagnetic shielding arise from the leading $O(\alpha^2)$ hyperfine shielding terms reflects the nature of the present systems that contain no heavy elements and possess the doublet spin state.

5. CONCLUSIONS

In the present study, the electron spin resonance parameters (g -tensor and hyperfine coupling) and paramagnetic nuclear magnetic resonance shieldings were predicted for the spin-1/2 paramagnetic defect models of graphenes. Hydrogenated and fluorinated graphenes with a single vacancy defect, $V_H@HG$ and $V_F@FG$, have an sp^2 -hybridized center with localized spin density. In these systems, due to the large energy gap, well-defined ESR g -values are obtained both as a function of k -sampling for a given supercell size and as a function of the system size and, hence, the defect concentration. Isotropic and anisotropic hyperfine couplings are large in the immediate vicinity of the paramagnetic center. It was demonstrated that

the ^{13}C pNMR shielding values are greatly magnified also for nuclei further away from the defect, an effect that may be observable in NMR experiments.

sp^2 -hybridized graphenes with chemisorbed hydrogen and fluorine adatoms, $H@G$ and $F@G$, feature long-ranged, delocalized, and slowly decaying spin density, which alternates between positive and negative signs due to the exchange polarization effect and the bipartite hexagonal lattice. The ESR hyperfine coupling tensors, calculated from the ground-state spin density, reflect the s -electron distribution with the isotropic Fermi contact and the p -electron distribution with the anisotropic dipolar coupling term. They converge fast with the system size. The pNMR shielding values are greatly magnified near the sp^3 -defect center but have large values also far from it. The only significant contributions to the hyperfine shielding, which is determined by the product $g \cdot A_K$ (see eq 2), arise from the two leading-order terms involving the free-electron g -factor, g_e . Higher order terms with Δg_{iso} and $\Delta\tilde{g}$ were omitted due to their negligible contributions and non-convergent behavior as functions of both system size and k -point sampling.

Although the predicted results for the magnetic resonance parameters contain errors arising from the semilocal DFT treatment, known to cause underestimation of the absolute value of the spin density as compared to hybrid DFT calculations,⁴⁴ the qualitative message of this work remains. Paramagnetic centers with doublet spin state in graphenes show distinct characteristics in their ESR and pNMR parameters. These spectroscopies may provide, with the help of first-principles modeling, detailed information about the type of vacancy or adatom defects as well as their density. We hope that the present predictions help in and encourage experimental verification.

■ ASSOCIATED CONTENT

Supporting Information

Further details of pNMR shielding, density of states plots, plots of anisotropic g -values as a function of supercell size, isotropic g -shift values and components perpendicular to and parallel with the plane of the material, and anisotropy of the paramagnetic ^{13}C NMR shielding tensor as a function of distance from the defect site, and tabulated values of the ESR and pNMR parameters. The Supporting Information is available free of charge on the ACS Publications website at DOI: 10.1021/acs.jctc.5b00402.

■ AUTHOR INFORMATION

Corresponding Authors

*(J.Vä.) E-mail: jarkko.vahakangas@oulu.fi.

*(J.Va.) E-mail: juha.vaara@iki.fi.

Funding

The research leading to these results has been obtained through funding from the People Programme (Marie Curie actions) of the European Union's Seventh Framework Programme FP7/2007-2013 under REA Grant Agreement No. 317127. We additionally thank the Academy of Finland for support within its directed programme in computational science and the University of Oulu Scholarship Foundation (J.Vä.) for funding.

Notes

The authors declare no competing financial interest.

■ ACKNOWLEDGMENTS

Computations were carried out at CSC-The Finnish IT Center for Science (Espoo, Finland) and the Finnish Grid initiative project.

■ REFERENCES

- (1) Yazyev, O. V.; Helm, L. *Phys. Rev. B: Condens. Matter Mater. Phys.* **2007**, *75*, 125408.
- (2) Boukhvalov, D. W.; Katsnelson, M. I.; Lichtenstein, A. I. *Phys. Rev. B: Condens. Matter Mater. Phys.* **2008**, *77*, 035427.
- (3) Şahin, H.; Ataca, C.; Ciraci, S. *Phys. Rev. B: Condens. Matter Mater. Phys.* **2010**, *81*, 205417.
- (4) Şahin, H.; Topsakal, M.; Ciraci, S. *Phys. Rev. B: Condens. Matter Mater. Phys.* **2011**, *83*, 115432.
- (5) Sofo, J. O.; Suarez, A. M.; Usaj, G.; Cornaglia, P. S.; Hernández-Nieves, A. D.; Balseiro, C. A. *Phys. Rev. B: Condens. Matter Mater. Phys.* **2011**, *83*, 081411(R).
- (6) Sofo, J. O.; Usaj, G.; Cornaglia, P. S.; Suarez, A. M.; Hernández-Nieves, A. D.; Balseiro, C. A. *Phys. Rev. B: Condens. Matter Mater. Phys.* **2012**, *85*, 115405.
- (7) Liu, H. Y.; Hou, Z. F.; Hu, C. H.; Yang, Y.; Zhu, Z. Z. *J. Phys. Chem. C* **2012**, *116*, 18193.
- (8) Santos, E. J. G.; Ayuela, A.; Sánchez-Portal, D. *New J. Phys.* **2012**, *14*, 043022.
- (9) Sepioni, M.; Nair, R. R.; Rablen, S.; Narayanan, J.; Tuna, F.; Winpenny, R.; Geim, A. K.; Grigorieva, I. V. *Phys. Rev. Lett.* **2010**, *105*, 207205.
- (10) Hong, X.; Cheng, S.-H.; Herding, C.; Zhu, J. *Phys. Rev. B: Condens. Matter Mater. Phys.* **2011**, *83*, 085410.
- (11) Nair, R. R.; Sepioni, M.; Tsai, I.-L.; Lehtinen, O.; Keinonen, J.; Krasheninnikov, A. V.; Thomson, T.; Geim, A. K.; Grigorieva, I. V. *Nat. Phys.* **2012**, *8*, 199.
- (12) McCreary, K. M.; Swartz, A. G.; Han, W.; Fabian, J.; Kawakami, R. K. *Phys. Rev. Lett.* **2012**, *109*, 186604.
- (13) Hong, X.; Zou, K.; Wang, B.; Cheng, S.-H.; Zhu, J. *Phys. Rev. Lett.* **2012**, *108*, 226602.
- (14) Eng, A. Y. S.; Poh, H. L.; Šaněk, F.; Maryško, M.; Matějčková, S.; Sofer, Z.; Pumera, M. *ACS Nano* **2013**, *7*, 5930.
- (15) Sun, P.; Wang, K.; Wei, J.; Zhong, M.; Wu, D.; Zhu, H. *Nano Res.* **2014**, *7*, 1507.
- (16) Banhart, F.; Kotakoski, J.; Krasheninnikov, A. V. *ACS Nano* **2011**, *5*, 26.
- (17) Candini, A.; Alvino, C.; Wernsdorfer, W.; Affronte, M. *Phys. Rev. B: Condens. Matter Mater. Phys.* **2011**, *83*, 121401(R).
- (18) Ugeda, M. M.; Brihuega, I.; Guinea, F.; Gómez-Rodríguez, J. M. *Phys. Rev. Lett.* **2010**, *104*, 096804.
- (19) Harriman, J. E. *Theoretical Foundations of Electron Spin Resonance*; Academic: New York, 1978.
- (20) Weil, J.; Bolton, J.; Welz, J. *Electron Paramagnetic Resonance: Elementary Theory and Practical Applications*; Wiley: New York, 1994.
- (21) Just, S.; Zimmermann, S.; Kataev, V.; Büchner, B.; Pratzner, M.; Morgenstern, M. *Phys. Rev. B: Condens. Matter Mater. Phys.* **2014**, *90*, 125449.
- (22) Ćirić, L.; Djokić, D. M.; Jaćimović, J.; Sienkiewicz, A.; Magrez, A.; Forró, L.; Šljivančanin, Z.; Lotya, M.; Coleman, J. N. *Phys. Rev. B: Condens. Matter Mater. Phys.* **2012**, *85*, 205437.
- (23) Rao, S. S.; Stesmans, A.; van Tol, J.; Kosynkin, D. V.; Higginbotham-Duque, A.; Lu, W.; Sinitskii, A.; Tour, J. M. *ACS Nano* **2012**, *6*, 7615.
- (24) Bertini, I.; Luchinat, C.; Parigi, G. *Solution NMR of Paramagnetic Molecules*; Elsevier: Amsterdam, 2001.
- (25) Vaara, J. In *High Resolution NMR Spectroscopy: Understanding Molecules and Their Electronic Structures*; Contreras, R. H., Ed.; Science and Technology of Atomic, Molecular, Condensed Matter & Biological Systems; Elsevier: Amsterdam, 2013; Vol. 3, p 41.
- (26) Riccò, M.; Pontiroli, D.; Mazzani, M.; Choucair, M.; Stride, J. A.; Yazyev, O. V. *Nano Lett.* **2011**, *11*, 4919.
- (27) Pickard, C. J.; Mauri, F. *Phys. Rev. Lett.* **2002**, *88*, 086403.
- (28) Pickard, C. J.; Mauri, F. *Phys. Rev. B: Condens. Matter Mater. Phys.* **2001**, *63*, 245101.
- (29) Blöchl, P. E. *Phys. Rev. B: Condens. Matter Mater. Phys.* **1994**, *50*, 17953.
- (30) Van de Walle, C. G.; Blöchl, P. E. *Phys. Rev. B: Condens. Matter Mater. Phys.* **1993**, *47*, 4244.
- (31) Blöchl, P. E. *Phys. Rev. B: Condens. Matter Mater. Phys.* **2000**, *62*, 6158.
- (32) Yazyev, O. V. *Nano Lett.* **2008**, *8*, 1011.
- (33) Moon, S.; Patchkovskii, S. In *Calculation of NMR and EPR Parameters: Theory and Applications*; Kaupp, M.; Bühl, M.; Malkin, V. G., Eds.; Wiley: Weinheim, Germany, 2004; p 325.
- (34) Pennanen, T. O.; Vaara, J. *J. Chem. Phys.* **2005**, *123*, 174102.
- (35) Vähäkangas, J.; Ikäläinen, S.; Lantto, P.; Vaara, J. *Phys. Chem. Chem. Phys.* **2013**, *15*, 4634.
- (36) Perdew, J. P.; Burke, K.; Ernzerhof, M. *Phys. Rev. Lett.* **1996**, *77*, 3865; *Phys. Rev. Lett.* **1997**, *78*, 1396. (erratum).
- (37) Giannozzi, P.; Baroni, S.; Bonini, N.; Calandra, M.; Car, R.; Cavazzoni, C.; Ceresoli, D.; Chiarotti, G. L.; Cococcioni, M.; Dabo, I.; Dal Corso, A.; de Gironcoli, S.; Fabris, S.; Fratesi, G.; Gebauer, R.; Gerstmann, U.; Gougousis, C.; Kokalj, A.; Lazzeri, M.; Martin-Samos, L.; Marzari, N.; Mauri, F.; Mazzarello, R.; Paolini, S.; Pasquarello, A.; Paulatto, L.; Sbraccia, C.; Scandolo, S.; Sclauzero, G.; Seitsonen, A. P.; Smogunov, A.; Umari, P.; Wentzcovitch, R. M. *J. Phys.: Condens. Matter* **2009**, *21*, 395502.
- (38) Vanderbilt, D. *Phys. Rev. B: Condens. Matter Mater. Phys.* **1990**, *41*, 7892.
- (39) Troullier, N.; Martins, J. L. *Phys. Rev. B: Condens. Matter Mater. Phys.* **1991**, *43*, 1993.
- (40) Monkhorst, H. J.; Pack, J. D. *Phys. Rev. B* **1976**, *13*, 5188.
- (41) Ruffieux, P.; Melle-Franco, M.; Gröning, O.; Biemann, M.; Zerbetto, F.; Gröning, P. *Phys. Rev. B: Condens. Matter Mater. Phys.* **2005**, *71*, 153403.
- (42) Cockayne, E. *Phys. Rev. B: Condens. Matter Mater. Phys.* **2012**, *85*, 125409.
- (43) Niyogi, S.; Bekyarova, E.; Hong, J.; Khizroev, S.; Berger, C.; de Heer, W.; Haddon, R. C. *J. Phys. Chem. Lett.* **2011**, *2*, 2487.
- (44) Kim, H.-J.; Cho, J.-H. *Phys. Rev. B: Condens. Matter Mater. Phys.* **2013**, *87*, 174435.